Journal of Drug Delivery Science and Technology 101 (2024) 106238

Contents lists available at ScienceDirect

Journal of Drug Delivery Science and Technology

journal homepage: www.elsevier.com/locate/jddst

Nanostructured lipid carrier formulation for delivering poorly water-soluble ITF3756 HDAC inhibitor

Marcelo Kravicz [a,*], Lorenzo Taiarol [a], Juliana S.R. Viegas [b], Giulia Sierri [a], Michele Mauri [c], Marcus Koch [d], Christian Steinkühler [e], Francesca Re [a]

[a] School of Medicine and Surgery, University of Milano-Bicocca, 20854, Monza, Italy
[b] Institute for Research and Innovation in Health, University of Porto, Portugal
[c] Department of Materials Science, University of Milano-Bicocca, Milano, Italy
[d] INM—Leibniz Institute for New Materials, Campus D2 2, 66123, Saarbrücken, Germany
[e] Italfarmaco SpA, 20092, Cinisello Balsamo, Italy

ARTICLE INFO

Keywords:
ITF3756
NLC
HDAC inhibitors
α-tubulin acetylation
Cancer

ABSTRACT

Histone deacetylases (HDACs) are enzymes that play crucial roles in cellular processes by hydrolyzing acetyl-L-lysine side chains in core histones, thereby regulating gene expression and maintaining homeostasis. Histone deacetylase inhibitors (HDACi) have emerged as promising agents, particularly in cancer treatment, due to their ability to induce cytotoxic and pro-apoptotic effects. Selective HDAC6 inhibitors, such as ITF3756, have shown low off-target toxicity and promising pharmacological activities, but their poor water solubility limits their application in nanoparticulate drug delivery systems. Here, we optimized a nanostructured lipid carrier (NLC) formulation for delivering ITF3756 using the design of experiments (DOE) and response surface methodology (RSM). An interaction between the factor surfactant and formulation volume was observed, thus demonstrating that the surfactant concentration impacts the NLC size. It can be speculated that the higher the amount of the drug in the formulation, the lower the polydispersion index (PDI), thus resulting in more stable nanostructures. The optimized ITF3756-NLC demonstrated a size of 51.1 ± 0.3 nm, 8.85 ± 4.71 mV charge, and high entrapment efficiency (EE%), maintaining stability for 60 days. Moreover, ITF3756-NLC enhanced α-tubulin acetylation in melanoma, lung, and brain cancer cell lines, indicating retained or improved bioactivity. The ITF3756-NLC formulation offers a viable approach for enhancing the bioavailability and therapeutic efficacy of HDAC6 inhibitors, demonstrating potential for clinical applications in cancer immunotherapy.

1. Introduction

HDACs are a family of enzymes found in different cellular compartments [1] and are notable for their role in the hydrolysis of acetyl-L-lysine side chains in the N-terminal region of core histones [2]. In this context, histone deacetylase inhibitors (HDACi) are considered promising therapeutic drugs as an alternative to chemotherapeutics [3] and are essential for homeostasis since they catalyse histone deacetylation [4].

ITF2357 (Givinostat), for instance, is an example of a second-generation synthetic pan-HDACi that belongs to the hydroxamic acids family and is active on most of the zinc-dependent HDAC family members with cytotoxic and pro-apoptotic effects [5,6]. Moreover, this pan-HDAC inhibitor has already been successfully incorporated into liposomes to improve its pharmacokinetics profile and brain delivery [7], with limitations that include a high clearance rate, lack of selectivity, and high toxicity compared to other selective inhibitors [7,8]. Also, HDACi were proven effective in some solid tumors [9–14], evidence that is also found for selective inhibitors [15–17].

A member of the class IIb HDACs is HDAC6, an α-tubulin and cortactin deacetylase involved in controlling microtubule and actin-dependent cell motility [18,19]. It is also involved in the clearance of misfolded proteins via aggresome formation and autophagy [20]. Furthermore, HDAC6 is highly expressed in various cancer types, such as glioblastoma [20], malignant melanoma, and lung cancer [18]. These features make HDAC6 a putative target for cancer treatment and neurodegenerative diseases.

Vergani et al., 2019 described the design and synthesis of a new class

* Corresponding author.
E-mail address: marcelo.kravicz@unimib.it (M. Kravicz).

https://doi.org/10.1016/j.jddst.2024.106238
Received 21 March 2024; Received in revised form 20 September 2024; Accepted 26 September 2024
Available online 28 September 2024

of potent and selective HDAC6 inhibitors (HDAC6i) bearing a pentaheterocyclic central core. Among them, ITF3756, a compound that showed remarkably low off-target toxicity both *in vitro* and *in vivo*, was able to increase regulatory T cell function at well-tolerated concentrations, thus suggesting a potential clinical use for the treatment of degenerative, autoimmune diseases and organ transplantation [21].

In a study by Ripamonti et al., 2019, the specific HDAC6 inhibitor ITF3756 showed *in vivo* and *in vitro* mechanisms whereby the drug increases the immune response, thus constituting a basis for the rational use of selective HDAC6 inhibitors for cancer immunotherapy [22]. Furthermore, ITF3756 resulted in specific HDAC6 inhibition by elevated tubulin acetylation with a 10-fold increase and low histone H3 acetylation with about a 3-fold increase after 60 min, providing evidence for *in vivo* selectivity of ITF3756 [12,21]. However, although ITF3756 offers promising pharmacological activities, its poor water solubility makes it challenging to incorporate into some nanoparticulate systems, such as liposomes. However, incorporating this HDAC6i into nanoparticles provides a tool to improve drug bioavailability, as previously reported with Givinostat [7]. Among the different approaches for improving the ITF3756 formulation, we propose an optimized ITF3756-NLC using the design of experiments (DOE) and RSM approaches.

NLCs are based on incorporating a drug into a mixture of solid and liquid lipids, thus providing a less or no crystalline matrix [23,24]. These nanostructures are considered a better alternative to other nanostructures, like solid lipid nanoparticles (SLN) [25–28], displaying a higher loading capacity for poorly water-soluble drugs than SLN [23]. Therefore, despite the mixture of a liquid and solid lipid, the higher amount of the latter enables the formation of nanoparticles [24], and properties such as size, PDI, and stability can be refined by changing the solid-lipid ratio in the formulation [29,30].

This study focused on optimizing a nanocarrier to deliver poorly water-soluble HDACi. The optimization produced a high-quality drug formulation without compromising the product's safety and effectiveness profile. Full Factorial Design and RSM were used to understand how input factors affect the final formulation (responses). As a result, optimized ITF3756-NLC with size and charge of 51.1 ± 0.3 nm and 8.85 ± 4.71 mV, respectively, showed the highest entrapment efficiency (EE%) and were stable for 60 days. In addition, the ability of ITF3756 to increase the α-tubulin acetylation was maintained, or at least improved, when embedded in NLC, as shown in A375, A549, and Gli36ΔEGFR-2 cell lines from melanoma, lung, and brain, respectively.

2. Materials and methods

2.1. Chemicals and materials

ITF3756 was synthesized and characterized by Italfarmaco S.p.A (purity >95 %). Precirol® ATO 5, Plurol Oleique® CC 497, Transcutol HP®, Peceol, Labrafil® M 2125, Labrafil® M 1944 CS, and Labrafac® Lipophile WL 1349 were kindly donated by Gattefosse (Lyon, France). Poloxamer (P407) was supplied by Sigma Aldrich. Gli36ΔEGFR-2, A375 and A549 cell lines were used as *in vitro* models of glioblastoma (GBM), melanoma and lung adenocarcinoma. Gli36ΔEGFR-2 were cultured as already been described [7]. A375 were kindly provided by Dr Domenico Mallardo (Istituto Nazionale per lo Studio e la Cura dei Tumori "Fondazione Giovanni Pascale), and A549 were purchased from American Type Culture Collection (ATCC).

2.2. Formulation of ITF3756-NLC

2.2.1. Determination of ITF3756 solubility in the lipid matrix

The solubility of ITF3756 in the solid and liquid excipients was checked by an established method [31,32]. Briefly, 10 mg of ITF3756 was mixed with the liquid excipients and agitated at 500 rpm to dissolve the drug. Then, an additional liquid lipid was added in parts to dissolve the ITF3756 to obtain a clear solution. Finally, suspensions were left at 65 °C for 24 h, and solubility was visually checked.

2.2.2. Preparation of ITF3756-NLC

The aqueous phase (AP) composed of P407 in PBS buffer and an ITF3756 stock solution in Transcutol HP® (8.1 mg/g) were previously prepared. An oil-in-water (O/W) emulsion was prepared by dispersing the pre-heated AP in the oily phase (OP), composed of solid lipid Precirol® ATO 5 (100 mg), liquid lipid Transcutol® HP (50 mg), and ITF3756 following the ratio drug-to-lipid (D/L) using ultrasonic irradiation (Vibra-Cell™ ultrasonic processor, 13 mm probe), in a one-step emulsification method followed by cooling the formulation in an ice bath.

2.2.3. Box–Behnken design (BBD) and ITF3756-NLC formulation optimization

ITF3756-NLC were developed and optimized according to a DOE strategy, and the BBD was performed with Design Expert Statistical Software (Stat-Ease version 22.3). The adopted independent variables were surfactant amount (A), D/L (B), sonication time (C), and formulation volume (D), and the dependent variables (responses) were particle size (Y1), PDI (Y2), charge (z-pot) (Y3), and EE% (Y4) (Table 1). The ITF3756-NLC were optimized according to the constraints of dependent variables: particle size and PDI in a range, z-pot as maximum (modulus), and the maximum EE%. Optimized ITF3756-NLC formulation was obtained after analyzing each response separately, establishing a model for each response using the same procedure with numerical and graphical optimization methods employing the desirability function technique to gather the responses (overlay graph and design space).

2.3. Characterization of ITF3756-NLC

2.3.1. Determination of particle size, polydispersity, z-pot, and NLC concentration

Particle size (hydrodynamic diameter, D_h) and PDI were determined by dynamic light scattering (DLS), and z-pot by electrophoretic mobility in an interferometric Doppler velocimeter (Brookhaven Instruments Corporation, Holtsville, NY, USA, equipped with ZetaPALS device) at RT, with a 652 nm laser beam and fixed angle of 90°. Samples were diluted in deionized water [33]. Purification and removal of unencapsulated ITF3756 were performed by ultrafiltration using an Amicon Ultra-15 10 kDa molecular weight cut-off (MWCO) (Millipore, Bedford, MA, USA) 4000×*g* for 30 min, and the drug EE% was determined by ultrafiltration using an Amicon Ultra - 0.5 10 kDa MWCO (Millipore, Bedford, MA, USA).

The free drug concentration in the concentrate collection tube was determined at OD270 using a NanoDrop™One UV–Vis Spectrophotometer (ThermoFisher Scientific™). The drug EE% in the nanoparticles was calculated according to Equation (1). The calibration curve for ITF3756 was obtained using PBS:DMSO 7.5 % (v/v) solutions in the concentration range 0.625–20 μg/mL ($R^2 = 0.99945$). The nanoparticle

Table 1
Independent and dependent factors of BBD of ITF3756-NLC.

Factors		Factor code	Level and range (coded)		
			−1	0	1
Independent	Amount of P407 (mg)	A	60	120	180
	D/L (μg/150 mg)	B	0.9	1.8	2.7
	Sonication time (minutes)	C	3	10	17
	Formulation volume (mL)	D	10	20	30
			constraints		
Dependent	Particle size (nm)	Y1	range		
	PDI	Y2	range		
	z-pot (mV)	Y3	maximum		
	EE (%)	Y4	maximum		

concentration of the optimized formulation was determined using a NanoSight NS300 (Malvern) after sample dilution in MilliQ® water.

$$EE\% = 100 \times \frac{ITF3756_{total} - ITF3756_{free}}{ITF3756_{total}} \quad \text{Equation 1}$$

2.3.2. ITF3756-NLC morphology via cryogenic electron microscopy (cryo-EM)

The morphology of the NLC and ITF3756-NLC was characterized by Cryo-EM as follows: An aliquot of 3 μL of the aqueous solution was applied to a holey carbon supporting TEM grid (Plano, Wetzlar, Germany, type S147-4), blotted for 2 s and plunge-frozen in liquid ethane using a Gatan (Pleasanton, CA, USA) CP3. A Gatan model 914 cryo-EM holder was used to transfer the grids to a JEOL (Tokyo, Japan) JEM-2100 LaB6 microscope. The cryo-EM micrographs were acquired at 200 kV accelerating voltage using a Gatan Orius SC1000 CCD camera operating under low-dose conditions.

2.3.3. Calorimetry

NLCs were also characterized by differential scanning calorimetry (DSC) using a DSC1 instrument from Mettler-Toledo equipped with a liquid nitrogen cooling unit and calibrated with indium metal standard. Aliquots of around 7 mg of each lyophilized formulation were freeze-dried to remove residual water and solvents while retaining the NLC shape and put into 40 μL aluminium pans. All measurements were performed using 80 mL/min nitrogen purge gas. Data analysis was performed with Stare software, v11.

2.3.4. ITF3756 release assay

The release studies were carried out using an inverse dialysis approach [34]. Briefly, 2.5 mL of ITF3756-NLC was added directly into a 60 mL dissolution medium (PBS pH 6.0 or 7.3). Then, a dialysis tube (Spectra-Por® Float-A-Lyzer® G2, 1500 μL, 20 kDa MWCO, previously activated in the vehicle) containing 1.5 mL of dissolution medium was immersed in the dissolution medium with 1 % w/v DMSO to maintain the sink conditions [35]. Then, at definite time intervals, a 100 μL sample was withdrawn from the dialysis tube and replaced with a fresh dissolution medium to maintain constant volume (1500 μL). Finally, the ITF3756 in the filtrate was quantified by UV–vis Nanodrop™ One.

2.3.5. Stability study of ITF3756-NLC

Stability studies of ITF3756-NLC and its unloaded NLC formulation without the drug were carried out to evaluate the size, charge changes, drug leakage during storage, and aggregation behavior. 3 mL of formulations were kept in closed vials and subjected to stability studies according to the International Council for Harmonisation (ICH) stability guidelines. The storage conditions were 4 °C, 25 °C, and 40 °C, and vials containing the formulations were sealed during the study. At different time intervals up to 60 days, the samples were withdrawn, visually examined, and analyzed in terms of particle size, PDI, and z-pot.

2.4. In vitro studies on cellular models

2.4.1. Cell lines

Gli36ΔEGFR-2 and A549 were maintained in Dulbecco's Modified Eagle Medium (DMEM), namely High Glucose without sodium pyruvate (ECM0101L, Euroclone, Milan, Italy) supplemented with 10 % (v/v) fetal bovine serum (FBS, ECS0180L, Euroclone, Milan, Italy), 4 mM L-glutamine (ECB3000D, Euroclone, Milan, Italy), and 1 % (v/v) penicillin/streptomycin (P/S) (ECB3001B, Euroclone, Milan, Italy). In addition, the A375 cell line was maintained in the same medium with added sodium pyruvate. All cell lines were maintained at 37 °C with 5 % CO_2 and saturated humidity.

2.4.2. Cell viability assay

The impact of empty NLC, free ITF3756, or ITF3756-NLC was evaluated through the MTT assay. In 96-well plates, 20,000 cells per well were seeded. Concentrations of NLC, ranging from 7.5 E10 to 150 E10 NP/mL, or ITF3756, from 0 to 10 μM, were introduced into the culture medium for 24 h. Following the manufacturer's protocol, the assay was conducted, and absorbance was measured at 570 nm using a microplate reader (SPECTROstar Nano, BMG LABTECH, Ortenberg, Germany). The results, representing the mean of three independent experiments ± SD, are expressed with untreated cells considered to have 100 % cell viability.

2.4.3. Immunoblot analysis

300,000 cells per well were seeded in a 6-well plate and treated with ITF3756-NLC (2.5 μM of ITF3756) for 24 h. Whole-cell lysates were obtained by washing cells twice in cold PBS and harvesting in 80 μL of radioimmunoprecipitation assay (RIPA) buffer (cat. no. 89901, ThermoFisher) supplemented with 1 % (v/v) of protease and phosphatase inhibitor cocktail (cat. no. 78446, ThermoFisher). Whole-cell lysates were quantified using a BCA Protein Assay Kit (cat. No. 23227, ThermoFisher) and separated by electrophoresis through precast gels (NuPAGETM 4–12 % Bis-Tris, 1.0 mm, Mini Protein Gel 15-wells, cat. No. NP0323, ThermoFisher). Proteins were transferred to nitrocellulose membranes using iBlotTM Transfer Stack (cat. No. IB301002, ThermoFisher), and membranes were blocked in 5 % (v/v) milk in TBS with 0.1 % (v/v) Tween-20 (TBST) for 1 h. Membranes were then incubated overnight at 4 °C with the following primary antibodies: Acetyl-α-Tubulin (5335, 1:1000) and α-Tubulin (2144, 1:1000), purchased from CST; and α-Actin (MA5-15739, 1:5000), purchased from ThermoFisher. Membranes were incubated with a secondary anti-rabbit antibody (A0545, 1:5000, Merck) or anti-mouse antibody (G21040, 1:20,000, Invitrogen) for 1 h at RT. Bands were detected using Immobilion ECL Ultra Western HRP Substrate (WBULS0100, Merck) under chemiluminescence using an Amersham Imager 600 (Cytiva, Marlborough MA, USA). Quantifications were made using ImageLab Software Version 6.1 (Bio-Rad).

2.5. Statistical analysis

All experiments were performed in triplicate. In the case of ITF3756-NLC optimization, data were analyzed with Design Expert software (Stat-Ease, Inc.) version 22.0.3. The analysis of variance was performed by one-way ANOVA. For biological tests, statistical analysis was performed with OriginLab using a *t*-test. Experimental data were expressed as mean ± SD, and statistical significance was considered at $p < 0.05$.

3. Results and discussion

3.1. Formulation ITF3756-NLC

ITF3756 is a promising drug candidate for cancer immunotherapy [20]. However, its poor water solubility makes it challenging to incorporate it into nanoparticulate systems to improve bioavailability and pharmacokinetics. Accordingly, the aim was to produce an NLC formulation to deliver ITF3756.

3.1.1. Determination of ITF3756 solubility in the lipid matrix

Drug solubility in lipid excipients is a critical factor for the EE% of a molecule in NLC. Therefore, determining ITF3756 solubility in lipid excipients was the first step to identifying suitable lipids to encapsulate the drug. Furthermore, the drug EE% can be controlled by changing the solid-lipid ratio and considering the molecule's solubility in the core matrix [29].

Plenty of solid lipids are available to form NLC, including triglycerides, mono and diglycerides, waxes, fatty acids, and alcohols [36]. Precirol® ATO 5 (glycerol palmitostearate) was used as a core matrix for the NLC formulations as it has a melting point of 50–60 °C (here established at 57.2 °C on first melting, Fig. 8S), lower than Compritol®

ATO (glyceryl dibehenate), a glyceride with a high melting point (65–77 °C). Integrating solid and liquid lipids in forming NLC reduces the matrix crystallinity, thus increasing the EE% and improving stability [36]. ITF3756 solubility was tested in some liquid excipients (data not shown). As Precirol® ATO 5 alone cannot solubilize the HDAC6i, Transcutol® HP was chosen as it showed the highest solubilization capacity and 1.2 g of Transcutol® HP was required to solubilize 10 mg of the drug (8.3 mg/g final concentration). Moreover, Transcutol® HP has high solvent properties and purity [37], it is approved by the U.S. Food and Drug Administration (FDA) for topical and transdermal routes, and is recommended by the manufacturer for a parenteral route, working as an enhancer of solubility [38].

3.1.2. Preparation of ITF3756-NLC

The Box-Behnken Design (BBD) provides a systematic and effective means for researchers to explore variable effects, identify critical factors, and attain desired properties in a streamlined fashion. Its efficiency lies in exploring three variable levels – low, medium, and high – enabling a comprehensive understanding of the response surface for identifying optimal conditions with fewer experimental runs compared to full factorial designs [39].

3.1.3. Box–Behnken design (BBD) and ITF3756-NLC formulation optimization

Designing pharmaceutical formulations, especially nanoparticle delivery systems, can be time-consuming and expensive. Several strategies based on process optimizations can be adopted to make this process faster, more accurate, and statistically explanatory. RSM are one of the most used methods to optimize preparation processes and understand the influences of variables on desired responses. One type of response surface model is the BBD, which provides an understanding of the influences of each factor and their linear, quadratic, and bidirectional interactions between factors. As well as this, quadratic results and the polynomial equation were used to optimize the nanoparticle system following pre-established goals [39]. Table 2 shows the formulation runs obtained by the BBD for the ITF3756-NLC with the independent and dependent factors (responses).

Some quadratic, linear, and two-factor models were applied, and the R-squared (R^2) was determined (Table 3). For an optimal design, the mixture of polynomials was reduced before the point selection, thus reducing the number of model points required by changing the selection criterion and selecting or clearing any term from the model. A reduced quadratic model was established to be the best-fitted model for the response Y1 size and Y2 PDI, with an R^2 of 0.9513 and 0.7956, respectively. Here, the predicted R^2 for both responses Y1 and Y2 were in reasonable agreement with the adjusted R^2, i.e., the difference is less than 0.2. Table 4 summarizes the ANOVA results for the response sizes (Y1) and PDI (Y2).

For the Y1 response size, the lack of fit (LOF) was significant due to the slight variation in the center points, being in the experimental runs where the independent factor is set halfway between, and in the center of the low and high settings. The presence of the center points to the design increases the probability of detecting significant factors and estimating the variability (or pure error). Although the predicted factorial model fits the model points well (providing a significant model fit), the differences between the actual data points are substantially more significant than the differences between the center points, thus providing a significant LOF statistic.

Table 3
R-squared (R^2) and other statistics after the ANOVA for the response particle size (Y_1) and PDI (Y_2).

response particle size (Y_1)			
Std. Dev.	5.05	**R^2**	0.9513
Mean	81.22	**Adjusted R^2**	0.9333
C.V. %	6.22	**Predicted R^2**	0.8494
		Adeq Precision	24.8022
response PDI (Y_2)			
Std. Dev.	0.0258	**R^2**	0.7956
Mean	0.1662	**Adjusted R^2**	0.7585
C.V. %	15.51	**Predicted R^2**	0.6373
		Adeq Precision	15.9464

Table 2
Box-Behnken experimental design for the ITF3756-NLC formulation selection. Independent factors are surfactant amount (A), in mg; (D/L) (B); sonication time (C), in min; formulation volume (D), in mL. Dependent factors (responses) are size (Y1) in nm, PDI (Y2), z-pot (Y3), mV, and EE% (Y4).

Formulations	Independent factors (X)				Dependent Factors (Y)			
	A	**B**	**C**	**D**	**Y_1**	**Y_2**	**Y_3**	**Y_4**
1	60	0.9	10	20	110.4	0.134	−0.86	40.12
2	120	0.9	10	30	69.2	0.137	10	52.28
3	120	2.7	3	20	71.4	0.145	−8.21	8.95
4	60	2.7	10	20	103.3	0.149	−4.69	29.7
5	180	1.8	10	10	97.9	0.3	−3.18	50.97
6	120	0.9	17	20	72.5	0.182	−7.99	17.72
7	120	1.8	10	20	70.4	0.131	−16.91	17.67
8	60	1.8	3	20	103	0.138	−9.36	24.12
9	60	1.8	17	20	106.6	0.155	−12.89	7.42
10	120	1.8	10	20	71.4	0.134	−8	17.78
11	120	0.9	10	10	98.6	0.286	−1.46	35.8
12	180	1.8	17	20	67	0.158	−7.88	44.26
13	180	1.8	3	20	57.6	0.152	−28.68	15.48
14	120	1.8	10	20	69.08	0.147	−16	15
15	120	2.7	10	10	76.4	0.164	−4.31	19.59
16	180	2.7	10	20	57.5	0.16	−12.41	30.74
17	180	0.9	10	20	55.3	0.142	−12.98	57.38
18	60	1.8	10	10	123	0.212	−7.98	12
19	120	2.7	10	30	66.3	0.151	−7.46	30.11
20	120	1.8	17	10	100.8	0.265	−8.53	28.96
21	120	1.8	3	10	99.5	0.256	−13.06	41.11
22	120	2.7	17	20	68.9	0.113	−5.33	28.97
23	120	0.9	3	20	69.7	0.134	−15.99	18.84
24	120	1.8	17	30	72	0.188	−19.97	34.78
25	120	1.8	3	30	68.7	0.134	−9.93	39.92
26	180	1.8	10	30	60.9	0.114	−5.73	44.42
27	60	1.8	10	30	105.5	0.106	−9.3	21.89

Table 4
ANOVA for reduced quadratic models. Response particle size (Y1) and PDI (Y2). p-values less than 0.0500 indicate that model terms are significant.

Source	Sum of Squares	df	Mean Square	F-value	p-value	
Response particle size (Y_1)						
Model	9462.99	7	1351.86	52.97	<0.0001	significant
A-P407	5444.28	1	5444.28	213.34	<0.0001	
B-D/L	84.80	1	84.80	3.32	0.0841	
D-volume	1966.08	1	1966.08	77.04	<0.0001	
AD	95.06	1	95.06	3.73	0.0687	
BD	93.12	1	93.12	3.65	0.0713	
A^2	1161.65	1	1161.65	45.52	<0.0001	
D^2	971.80	1	971.80	38.08	<0.0001	
Residual	484.86	19	25.52			
Lack of Fit	482.15	17	28.36	20.94	0.0465	significant
Pure Error	2.71	2	1.35			
Cor Total	9947.85	26				
Response PDI (Y_2)						
Model	0.0569	4	0.0142	21.41	<0.0001	significant
B-D/L	0.0015	1	0.0015	2.22	0.1504	
D-volume	0.0355	1	0.0355	53.51	<0.0001	
BD	0.0046	1	0.0046	6.96	0.0150	
D^2	0.0152	1	0.0152	22.95	<0.0001	
Residual	0.0146	22	0.0007			
Lack of Fit	0.0145	20	0.0007	10.00	0.0947	not significant
Pure Error	0.0001	2	0.0001			
Cor Total	0.0715	26				

Fig. 1S and 2S (Supplementary Information) show the diagnostic plots with internally studentized residuals for the responses Y1 size and Y2 PDI. The normal probability plot indicates a normal distribution of the residuals, thus following a straight line. Also, a random scatter in the residuals versus predicted responses checks for lurking variables that may have influenced the responses during the experiment. To detect a value that is not easily predicted by the model, the plot predicted versus actual responses was provided.

3.1.3.1. Effect of independent variables on the particle size of ITF3756-NLC. ITF3756-NLC size was highly influenced by the surfactant amount and the formulation volume (Fig. 1). Smaller particles were obtained with the highest surfactant concentration, as seen in Fig. 1a. An interaction between the factor surfactant (A) and formulation volume (D) (Fig. 1b) was observed ($0.05 \leq p < 0.1$) supported by the effect plots in a normal plot of residuals between the normal probability (%) and the internally studentized residuals, and the residuals versus predicted diagnostic plot for the response Y1 size (Fig. 1S, Supplementary Information), thus suggesting that the surfactant concentration impacts the NLC size and the volume.

For instance, the formulations with the same surfactant concentration, i.e., 60 mg surfactant in a final volume of 10 mL and 180 mg of surfactant in 30 mL volume (final concentration of 6 mg/mL), had different size profiles. The smallest NLC sizes were obtained with 180 mg of surfactant in 30 mL. AA and DD interactions were significant, i.e., quadratic effects of surfactant amount and volume, respectively ($p < 0.05$). Agrawal et al., 2019 reported that an increase in surfactant concentration initially resulted in a considerable decrease in the nanoparticle size due to a reduction in the interfacial tension and created steric hindrance on the NLC surface [40,41]. In our study, the presence of the surfactant created steric hindrance on the particle surface, which protected the minor particles from coalescence into larger particles, but the size was strongly influenced by the volume. It is possible that the lipid molecules of the NLC might re-arrange and reassemble to form smaller nanoparticles under suitable probe-sonication conditions because of NLC fluidity [42]. As the formulation volume changed but the surfactant was maintained, the ratio between sonication power and volume was not constant, and this provided nanoparticles with different size profiles [43,44]. Equation (2) provides the impact of independent factors and their interactions on the response Y1 size and was used to generate the 3D response surface graphs, which use ANOVA graphics to elucidate variable influences on the response. Table 1S (Supplementary Information) shows the coefficients in terms of coded factors for the response Y1 size.

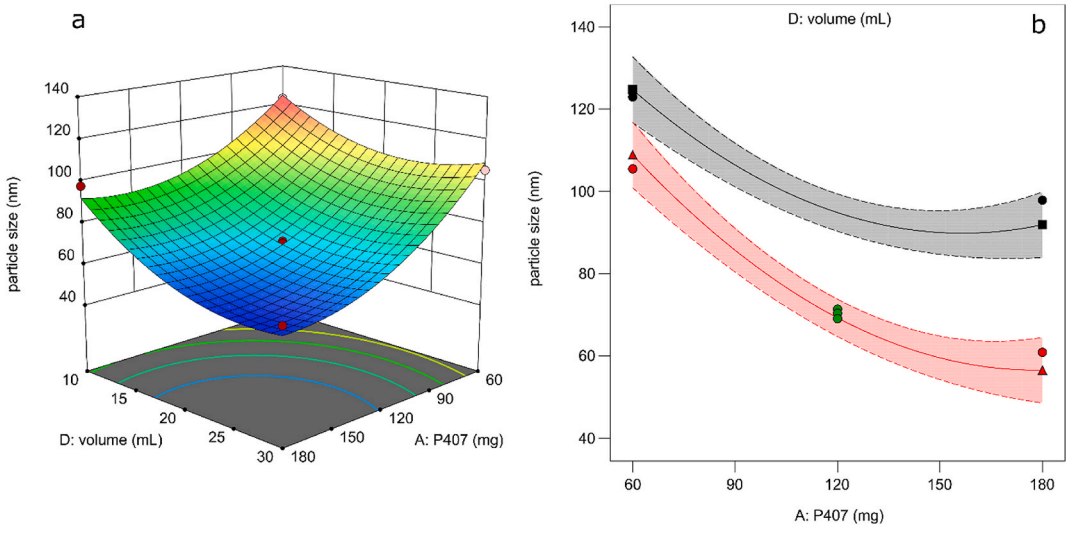

Fig. 1. Effect of surfactant amount and formulation volume on particle size. 3D surface plot representations (a) of the response particle size (Y1) plotted against combinations of the numeric factors A (surfactant, mg) and D (formulation volume, mL). The numeric factor B (drug-to-lipid ratio) was kept at 0.18. Particle size response Y1 varies from blue to red, 55.3–123 nm, respectively. Interaction graphs (b) of factors A (surfactant, mg) versus D (formulation volume, mL) in the level (0) corresponding to D/L 0.9 for the numeric factor B (drug-to-lipid ratio). Particle size is represented by the gray area around the black square symbol (formulation volume 10 mL) and the reddish area around the red triangle symbol (formulation volume 30 mL). Round black and red symbols represent the design points. Green symbols represent the central points. Dashed lines represent the 95 % confidence interval (CI) bands. (For interpretation of the references to colour in this figure legend, the reader is referred to the Web version of this article.)

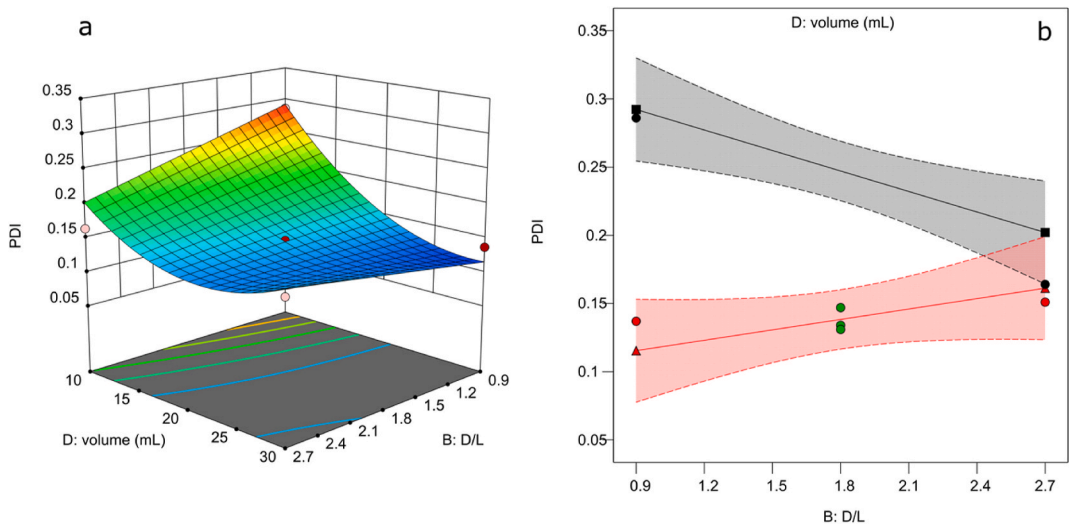

Fig. 2. Effect of D/L ratio and formulation volume on particle PDI. 3D surface plot representation (a) of the response PDI (Y2) plotted against combinations of numeric factors X2 (drug-to-lipid ratio) and D (formulation volume, mL). The numeric factor A (surfactant, mg) was kept at 180 mg. PDI response Y1 varies from blue to red, 0.106 to 0.3, respectively. Interaction graphs (b) of factors A (surfactant, mg) versus D (formulation volume, mL) in the levels (−1), (0), and (+1) of the numeric factor B (drug-to-lipid ratio), (d) 0.9, (e) 2.7, and (f) respectively. PDI is represented by the gray area around the black square symbol (formulation volume 10 mL) and the reddish area around the red triangle symbol (formulation volume 30 mL). Round black and red symbols represent the design points, and green symbols represent the central points. Dashed lines represent the 95 % CI bands. (For interpretation of the references to colour in this figure legend, the reader is referred to the Web version of this article.)

$$Y1(size) = 69.75 - 21.30A - 2.66B - 12.80D - 4.88AD + 4.82\,BD + 13.47A^2 + 12.32D^2$$

Equation 2

3.1.3.2. Effect of independent variables on the PDI of ITF3756-NLC. For the response PDI (Y2) (Fig. 2a), the formulation volume (D) had a significant effect on the response, in which the highest level of D provided the lowest PDI values. It can also be observed that the lipid phase influenced the PDI, as the total lipid concentration (Precirol® plus Transcutol® HP) changes from the lowest level of D (15 mg/mL) to the highest D level (5 mg/mL). PDI increases as the lipid phase concentration increases (Fig. 2b). A significant interaction between the factor D/L (B) and formulation volume (D) was also found (p-value 0.0150), even though the factor B alone was not significant (p-value 0.1504). It can be speculated that the higher the amount of the drug in the formulation, the lower the PDI, thus resulting in a more stable nanostructure. DD interaction, i.e., quadratic effects of volume, was significant ($p < 0.05$).

Pimentel-Moral et al. [45] showed that surfactant and lipid phase concentrations impact particle size and PDI, the latter associated with long-term stability when PDI indicates a narrow distribution ~ 0.1. Formulation volume as a factor was included in this study to evaluate the formation of the NLC by changing the concentration of all components. However, the concentration of surfactant and lipids from the core matrix and the drug were not kept with the changes in volume. Therefore, the impact of volume on NLC formulations and the power density (sonication parameter) as a factor deserve further study.

The factor D volume influences the response Y2 PDI and is associated with an interaction with the factor B D/L, even though the response Y2 was not significant for B (p-value 0.1504) (Table 4). For the 10 mL formulation, higher PDI values were found for the D/L 0.9 compared to the 30 mL formulation volume. This difference at D/L 2.7 is lower for both formulation volumes and, as mentioned before, the formulation volume significantly influenced the response Y1 size, supported by the effect plots in a normal plot of residuals between the normal probability (%) and the internally studentized residuals, and the residuals versus predicted diagnostic plot for the response Y2 PDI (Fig. 2S, Supplementary Information). Equation (3) provides the impact of independent factors and their interactions on the response Y2 PDI and was used to generate the 3D response surface graphs and contour plots (Fig. 3A), which utilize ANOVA graphics to elucidate variable influences on the response. Table 1S (Supplementary Information) shows the coefficients in terms of coded factors for the response Y2 PDI.

$$Y2(PDI) = 0.1449 - 0.0111B - 0.0544D + 0.0340BD + 0.0478D^2$$

Equation 3

3.1.3.3. Effect of independent variables on z-pot and EE% of ITF3756-NLC. Tables 2S and 3S (Supplementary Information) summarize the ANOVA results, R-squared (R^2), and the coded factor coefficients for the response charge (Y3) and EE% (Y4). Even though a model can be obtained for the response charge Y3 ($p < 0.05$), the predicted R^2 of 0.0701 was not as close to the adjusted R^2 of 0.3702 as normally expected, i.e. the difference is more than 0.2. Consequently, this response was not used in further optimization during this study, as it may indicate a large block effect. In the case of the response EE% Y4, a significant model was obtained, and the factor A surfactant amount was significant ($p < 0.05$). Also, the predicted R^2 of 0.2030 was in reasonable agreement with the adjusted R^2 of 0.3949 (the difference between them is less than 0.2), but the R^2 for both models (Y3 and Y4) was lower than 0.6, and consequently, these models were not used to navigate in the overlay plot (optimization of ITF3756-NLC).

3.1.3.4. Optimization of ITF3756-NLC. Fig. 3A represents the overlay plot indicating a bright yellow region as the design space with the flagged point as the optimum ITF3756-NLC formulation with its composition and responses. The bright yellow on the plot shows where the entire range intervals meet the criteria, and the dark gold corresponds to where the point estimate meets the criteria requirements. An estimation interval was added to the graphical overlay plot to help understand the impact of uncertainty on achieving size and PDI goals. In the search for the optimized formulation and validation of the experimental design, the optimum ITF3756-NLC formulation was determined with the assistance of the numerical optimization method employing the desirability function technique (Fig. 3B), gathering the response size Y1 and PDI Y2, in which the goals were the range of particle sizes between 55.3 and 80 nm, and PDI in the range of 0.106 and 0.2, with an interval of confidence (one-sided) of α 0.05. For this goal, a desirability of 1 was

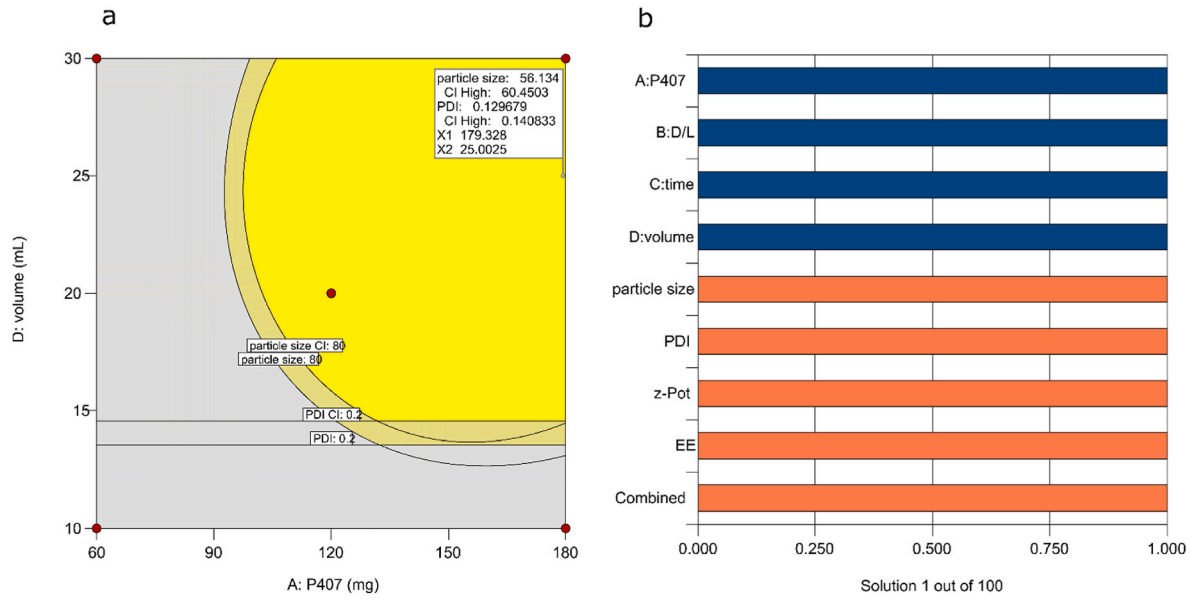

Fig. 3. Overlay of contour plots (a) from the response particle size (Y1) and PDI (Y2) and desirability (b). The numeric factors displayed are A (surfactant, mg) and D (formulation volume, mL). The numeric factors B (D/L) and C (time) were kept at 1.8 and 3 min, respectively. The bright yellow on the plot shows where the entire range intervals meet the criteria, and the dark gold corresponds to where the point estimate meets the criteria requirements. An estimation interval (one-sided, α 0.05) was added to the graphical overlay plot to help understand the impact of uncertainty on achieving size and PDI goals. The flagged window shows the "optimal location" where the specifications are achieved. (For interpretation of the references to colour in this figure legend, the reader is referred to the Web version of this article.)

achieved.

The four independent factors A to D were set at 180 mg for the amount of P407 used as a surfactant in the formulation, a D/L of 0.9 (135 μg of ITF3756 in 150 mg of total lipid composition), 3 min of sonication, and 25 mL of formulation volume. To prepare the optimized ITF3756-NLC, a simple emulsification method followed by probe sonication was used. Confirmation runs were needed and carried out (Table 5) to validate the experimental results and the significant lack of fit (LOF). These additional runs were conducted at the optimal settings, and the average of the runs was compared to the prediction interval (PI). The PI generated from similar experiments contained the average of the future sample. The final coefficients regarding coded factors Y1 size and Y2 PDI are presented in Table 1S (Supplementary Information) and confirmation runs were performed to validate the experimental results and the LOF (Table 5). These additional runs were conducted at the optimal settings, and the average of the runs was compared to the prediction interval (PI). The PI generated from similar experiments contained the average of the future sample.

3.2. Characterization of ITF3756-NLC

3.2.1. Determination of particle size, polydispersity, z-pot and NLC concentration

The physicochemical features of the ITF3756-NLC and unloaded NLC are presented in Table 6. They showed a mean particle size lower than 60 nm with a PDI <0.2, thus indicating the low-medium dispersity of the nanoparticles, and the EE% was higher than 50 %. The final formulation volume after purification was 6.9 mL, thus providing a 10.3 mg/mL (34 μM) ITF3756 concentration, suitable for *in vitro* and *in vivo* assays. The incorporation of ITF3756 did not significantly affect the physicochemical features of NLC, at least not immediately after preparation.

Table 6
Physicochemical properties of optimized ITF3756-NLC and plain NLC.

	D_h, nm ± SD	PDI (SD)	ζ, mV ± SD	EE % ± SD	NP mL^{-1} ± SD
NLC	52.1 ± 0.5	0.16 ± 0.005	−8.85 ± 4.71	NA	$4.82 \times 10^{12} \pm 0.85 \times 10^{9}$
ITF3756-NLC	50.1 ± 0.3	0.14 ± 0.012	−17.7 ± 4.71	52.38 ± 2.7	$5.24 \times 10^{12} \pm 1.1 \times 10^{9}$

3.2.2. ITF3756-NLC morphology via cryogenic electron microscopy (cryo-EM)

The morphology of optimized ITF3756-NLC and unloaded NLC was investigated via Cryo-EM. This technique enabled the visualization of the NLC morphology dispersed in water (Fig. 4), resulting in images of complex 3D structures with different orientations. In this study, ITF3756-NLC and unloaded NLC shapes appear discoid from the top view and elliptic-like or rodlike shape from the side view, they appear more electron-dense, and a similar morphology to what has been previously reported [46]. As observed in other studies, the nanoparticle sizes and thickness are between 10 and 40 nm [47], and the nanoparticle thickness was generally between ≈5 and 40 nm, a challenging measurement due to the tilt of the particles. In our study, unloaded NLC and ITF3756-NLC showed a discoidal morphology and an elliptic shape, with there being no significant difference between the unloaded NLC and the drug-loaded nanoparticles. Similar morphology was observed for NLC in

Table 5
Confirmation run conducted at the optimal settings. Two-sided, confidence = 95 %. The table reports predicted values with their SD, N, SE (standard deviation associated with the prediction of a mean value), and 95 % confidence intervals. Data Mean are values deriving from sample preparations.

	Predicted Mean	SD	N	SE Pred	95 % PI low	Data Mean	95 % PI high
D_h	56.4148	5.05162	3	4.31685	47.3795	**50.1333**	65.4501
PDI	0.123762	0.0257691	3	0.0189838	0.0843926	**0.14**	0.163132

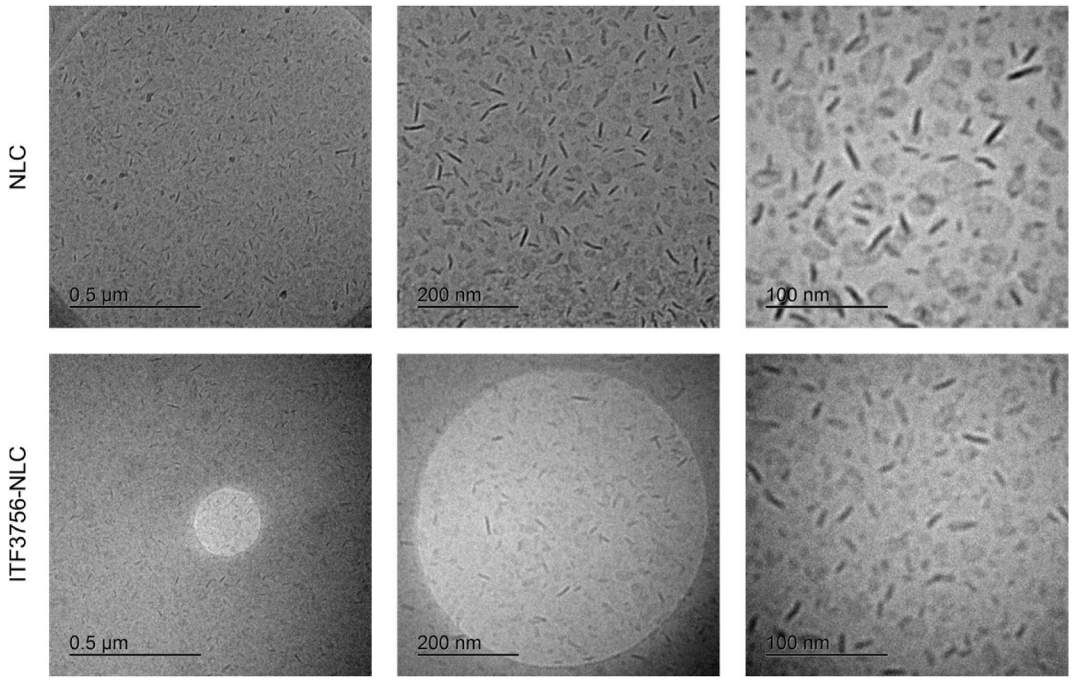

Fig. 4. Cryo-EM images of NLC and ITF3756-NLC. Scale Bar corresponds to 500, 200, and 100 nm.

previously published studies [48].

3.2.3. Calorimetry

DSC is a technique that offers a close look at the melting and crystallization behaviour of crystalline material, such as lipid nanoparticles, so as to characterize the physical and also chemical changes in their enthalpy. Here, the heat capacity of the lipid DSC was used to explore the particle morphology and stability of ITF3756-NLC and its phase transitions. Samples were heated from 20 °C up to 85 °C and kept for 15 min at 85 °C, then cooled down to 20 °C, and kept at 20 °C for 15 min, and finally heated up to 150 °C and cooled down to 20 °C. All dynamic steps were performed at 5 °C/min. As expected for complex nanoparticles, the thermogram is quite rich and differs from the simple linear combination of the components. Full thermograms are provided in the Supplementary Information (Figs. 6S–10S), and Fig. 5 highlights the most relevant difference between the ITF3756-NLC and unloaded NLC, namely the endothermal events associated with the first heating ramp.

ITF3756-NLC are dominated by a single endothermal event near 51 °C, consistent with nanoparticles composed mainly of Precirol, whose melting point (56.7 °C) is lowered by being mixed with Transcutol, a liquid at RT (Fig. 6S, Supplementary Information. A contribution from P407 is also possible since it has a melting point of around 57.4 °C (Fig. 7S, Supplementary Information). The presence of Transcutol is also reflected by a decrease in melting enthalpy, displayed in Table 7. Instead, the NLC particles have two separate peaks, one at 45 °C the other closer to 55 °C.

The second heating ramp is remarkably similar for both samples (Fig. 8S and 9S, Supplementary Information). This second ramp describes the fusion of components that have been melted and recrystallized in the DSC in the same condition and is more responsive to differences in composition. Since the second and subsequent ramps are similar, differences in the first ramp can be attributed to the structure of both ITF3756-NLC and unloaded NLC, not to their composition. A possible explanation is that, while the particles have the same shape regardless of the presence of the drug, the unloaded NLC displays a local nanophase separation, resulting in the formation of domains richer in Transcutol and others closer to a pure Precirol/P407 mixture. The presence of domains with a lower melting point also explains the

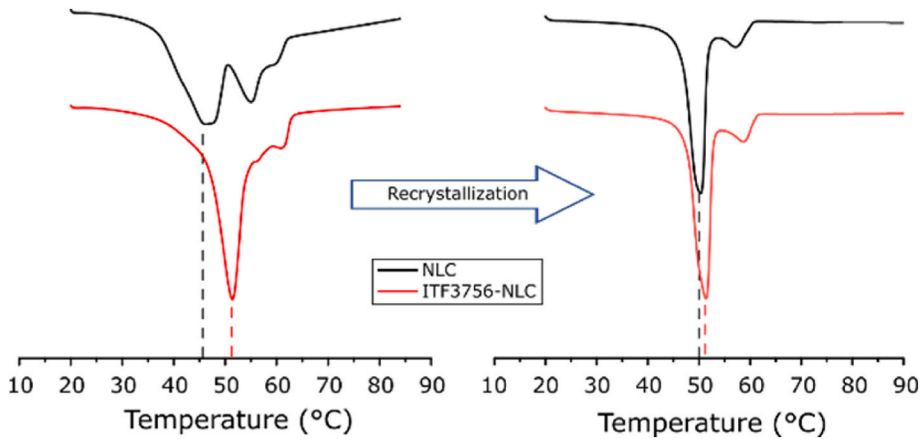

Fig. 5. DSC trace of the first heating ramp spanning from 25 °C to 85 °C and in the same range as the second. The baseline is shifted for comparison. Differences in the first heating ramp are evident but are much reduced during the second.

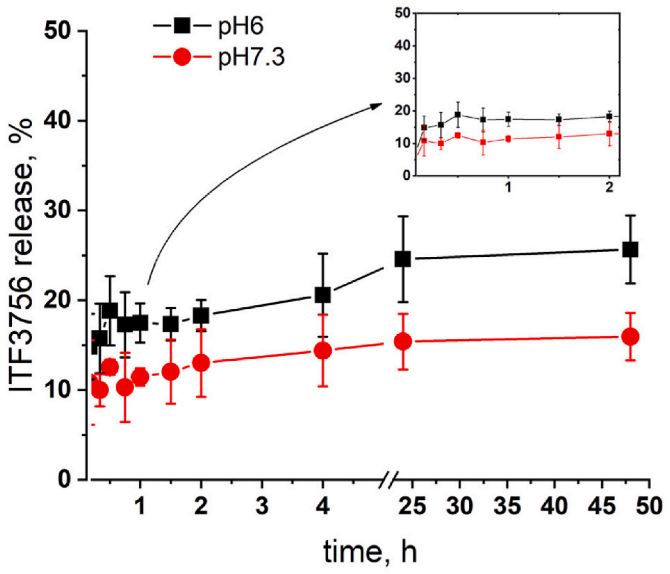

Fig. 6. Release profile of ITF3756 over time, using a dialysis method (dialysis membrane 20 kDa MWCO). The drug release was measured at 37 °C in PBS Buffer at two different pH values, 6 and 7.3. ITF3756 was quantified by UV–vis.

reduced temporal stability of the unloaded NLC at 25 °C: those regions are so close to Tm that they can promote particle aggregation upon collision. The onset of the endothermal events displayed by NLC is lower than 40 °C. Particles stored at that temperature endure an annealing process that extends their lifetime.

The structural difference cannot be attributed to the contribution of the drug, which has a melting point of around 75 °C (Fig. 10S, Supplementary Information). With around 1 % w/w in the formulation, the direct contribution of ITF3756 to the endothermal events is negligible, especially considering that its melting enthalpy is around 1.4 J/g, compared with the values of the solid components, which are over 100 J/g. Indirect effects are instead possible: the formation process of NPs is very delicate since the possible structures are often energetically similar from a thermodynamics point of view. As such, small amounts of selected nucleating agents [49,50], or even residual solvents, can direct a crystallization or self-assembly towards the desired form. Here, the drug's presence helps obtain an intimate mixing of the components, thus increasing the particle viability. ITF3756-NLC have some regions with a melting temperature closer to RT, possibly softer and even sticky regions, thus favoring aggregation processes whenever particles collide due to their random motion in the dispersion. Instead, with a single melting peak at higher temperatures, the particles loaded with the drug tend to bounce from each other, at least at RT.

3.2.4. *ITF3756-NLC release assay*

As the release behaviour depends on the drug solubility in the lipid phase [51], the *in vitro* release of ITF3756 from NLC was evaluated (Fig. 6). Optimized ITF3756-NLCs were tested in PBS pH 6 and 7.3 to mimic the acidic pH of tumor microenvironments and physiological pH, respectively. A rapid release of ITF3756 over the first hour was observed with 25.6 ± 3.78 % and 13.9 ± 2.7 % for pH 6 and 7.3, respectively, in 48 h. As a free drug, ITF3756 diffuses across the dialysis membrane (Fig. 4S, Supplementary Information), although a co-solvent such as DMSO is needed in the dissolution medium to maintain the sink conditions followed by sustained release up to 25.6 ± 3.78 % and 13.9 ± 2.7 % for pH 6 and 7.3, respectively, in 48 h. This result demonstrates that the ITF3756-NLC exhibited an initial fast release followed by a sustained release phase, as observed in other NLC-based studies [46,47]. Such a fast release may significantly change the therapeutic outcome *in vivo* in future studies employing the cell models proposed in our study, as observed by a recent study [52].

Even though the drug is loaded into the NLC, it is not always uniformly solubilized in the lipid matrix and is localized in various parts of the nanoparticle [53]. Starting from our previous studies of Givinostat [7], we tried to incorporate ITF3756 in a liposome formulation (Fig. 3S, Supplementary Information) without success. Even with a high EE%, a fast drug release of ITF3756 from liposomes (Fig. 5S, Supplementary Information) was observed in 4 h, which limited the applicability of ITF3756-liposomes. The release results obtained with ITF3756-NLC

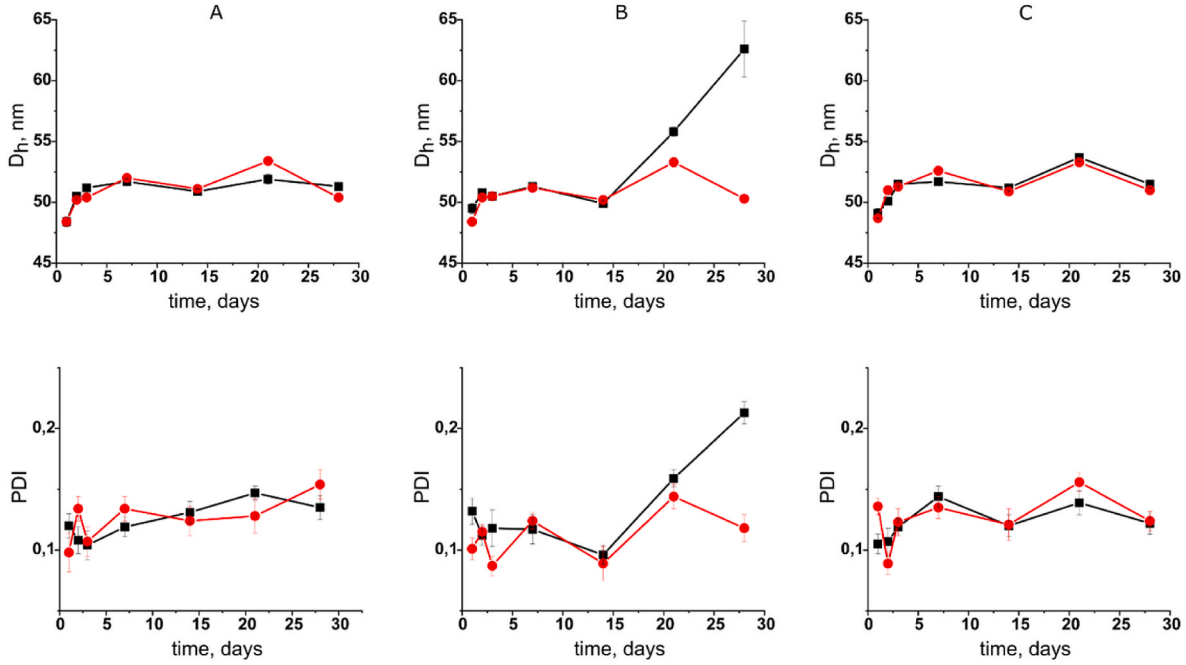

Fig. 7. NLC and ITF3756-NLC stability at (A) 4 °C, (B) 25 °C, and (C) 40 °C for 30 days. Nanoparticle size (Dh) and PDI are shown. Black symbols represent NLC without ITF3756, and red symbols are ITF3756-NLC. After 60 days, the size and PDI of the ITF3756-NLC at 4 °C and RT did not change (size 52–55 nm and PDI <0.2). (For interpretation of the references to colour in this figure legend, the reader is referred to the Web version of this article.)

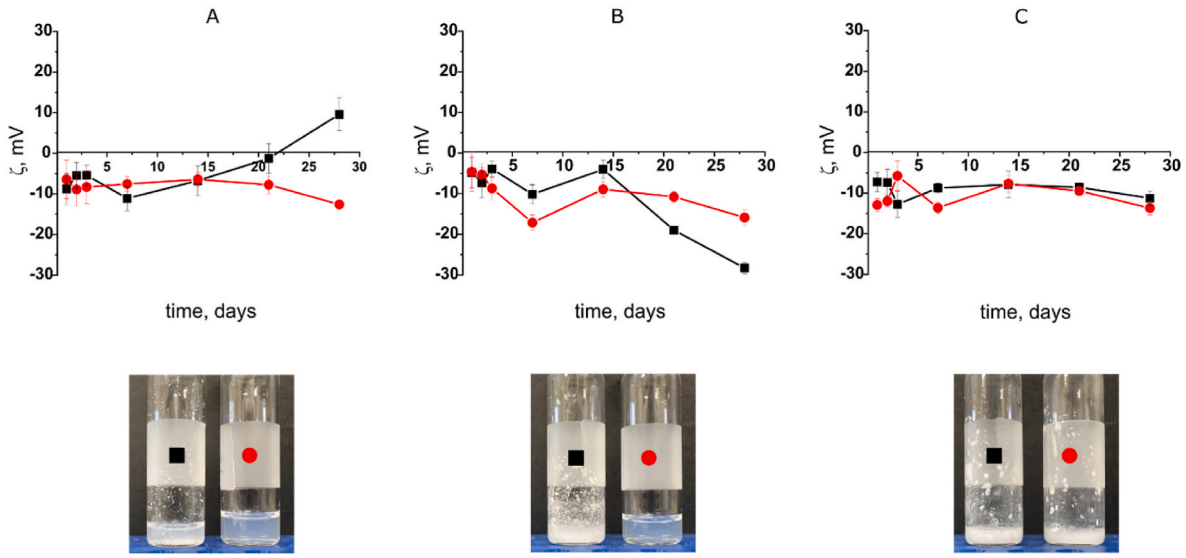

Fig. 8. NLC and ITF3756-NLC stability at (A) 4 °C, (B) 25 °C, and (C) 40 °C for 30 days. Nanoparticle charge is shown. Black symbols represent NLC without ITF3756, and red symbols are ITF3756-NLC. After 60 days, charge of the ITF3756-NLC at 4 °C and RT did not change (z-pot between −10 and −15mV). Samples were agitated to see aggregation. (For interpretation of the references to colour in this figure legend, the reader is referred to the Web version of this article.)

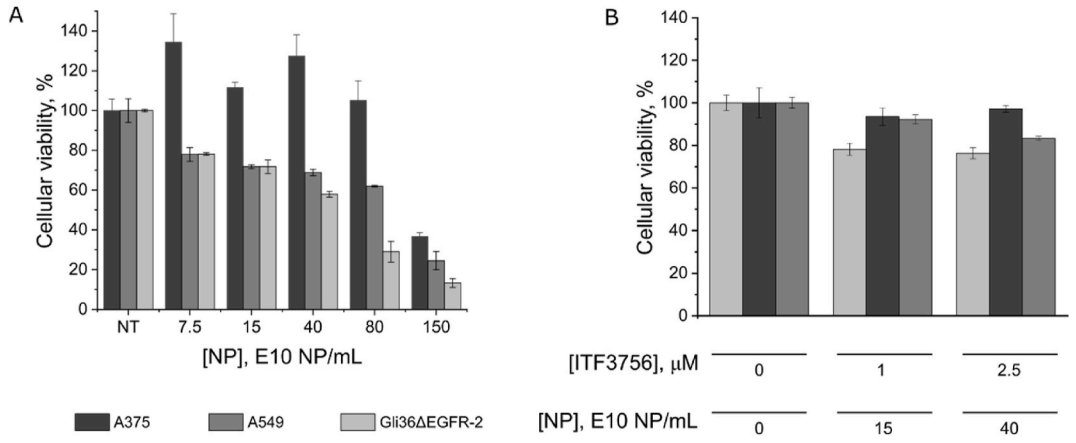

Fig. 9. Cell viability via MTT assay. (A) Impact of unloaded NLC on A375, A549, and Gli36ΔEGFR-2. (B) At 40 E10 NP/mL concentration, ITF3756-NLC provided cell viability higher than 50 %. Cells were treated for 24 h. Results were normalized for the non-treated cells, and NT corresponded to 100 % cellular viability.

agree with the already reported higher NLC loading capacity and stability [54] compared to liposomes. ITF3756 NLC released about 25 % in 48 h, while the remaining amount of ITF3756 is supposed to be incorporated into the NLC, especially in the liquid phase inside the NLC, stabilizing the particles, as shown by the DSC results.

Generally, drug release studies of nanoparticles of poorly water-soluble drugs are performed in suboptimal conditions [55], in which, for instance, the nanoparticles are not sufficiently diluted. Thus, drug release from the carrier is potentially underestimated and leads to inaccurate predictions [49], even when using small-pore-sized membranes that can solve one of the major limitations of other *in vitro* drug release techniques [56]. As ITF3756 cannot exert a therapeutic effect while encapsulated, the ITF3756-NLC should hold the HDAC6i stable until it reaches the target location and promptly releases its drug cargo to achieve a therapeutic concentration [57].

3.2.5. Stability study of ITF3756-NLC

Temperature is considered one of the factors involved in nanoparticle stability [58], which can be evaluated by following the changes in the nanoparticle size, dispersion, and zeta potential for unloaded NLC and ITF3756-NL. Fig. 7 shows the size and PDI of unloaded NLC and ITF3756-NLC at 4 °C, 25 °C, and 40 °C. Optimized ITF3756-NLC and unloaded NLC stored at 4 °C (Fig. 7A) had comparable size and PDI during 30 days of storage. However, unloaded NLC after 15 days had a higher charge than ITF3756-NLC, thus suggesting a destabilization of the formulation (Fig. 8A). Absolute charge values present the degree of repulsion between nanoparticles in the formulation, resulting in the prevention of particle aggregation during storage [59], and samples with a zeta potential of −15 mV or higher tend to show gelation phenomena [59,60].

At 40 °C, both unloaded NLC and ITF3756-NLC were stable for 30 days, thus showing that the drug did not affect the nanocarriers' stability at this temperature (Fig. 8C). However, at 25 °C (Fig. 7B), unloaded NLC kept their size and PDI similar to the ITF3756-NLC until 15 days of storage. As previously reported, this difference in the stability behavior between the ITF3756-NLC and unloaded NLC can be explained by the nanostructure core liquid lipid inhibiting polymorphic phase changes [61].

These phase changes may be combined with the presence of the ITF3756 in the NLC core, thus increasing the inhibition of the polymorphism changes and drug extrusion. After 60 days, the size, PDI, and charge of the ITF3756-NLC at 4 °C and 25 °C did not change (size 52–55

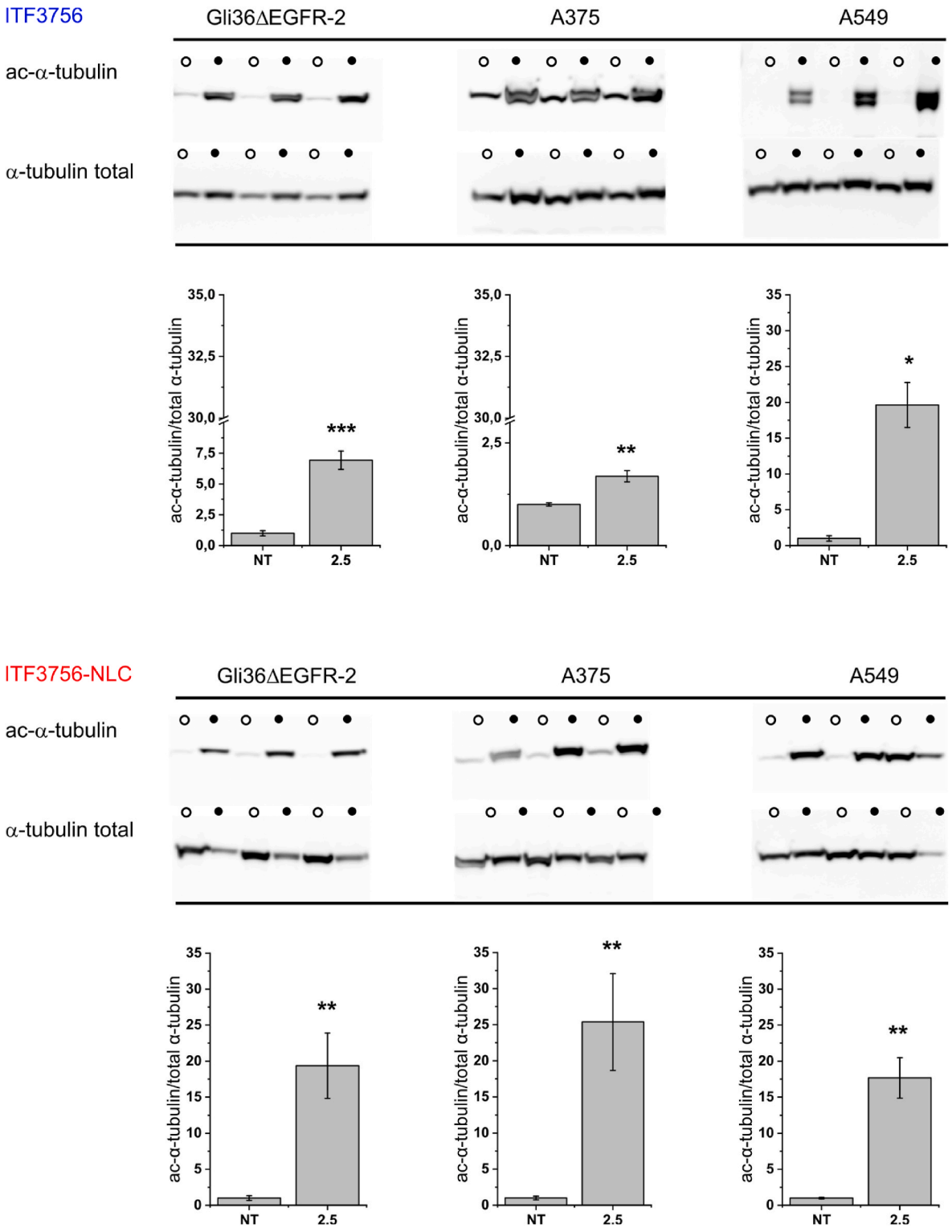

Fig. 10. Levels of α-tubulin expression. WB analysis shows the protein expression after 24 h treatment with 2.5 μM ITF3756 and ITF3756-NLC. Untreated cells (NT) were used as control. Data are presented as mean ± SD. ○ symbol, NT cells; ● symbol, 2.5 μM ITF3756 as free drug or in ITF3756-NLC. **p < 0.01 by Student's t-test.

nm, PDI <0.2, and z-pot between −10 and −15mV), even though the lower temperature might lead to polymorphism transition of lipid matrix then recrystallization [62]. This explains the charge values lower than −10mV at 25 °C, which provide a more stable NLC with the presence of the drug in the ITF3756-NLC formulations at the two temperatures for up to 60 days.

Moreover, the electric charge on the particle surface may be maintained with enough repulsive interaction to sustain the system's stability [62,63], after which, the size and PDI of the unloaded NLC increase. Interestingly, this event did not occur for ITF3756-NLC, suggesting that the drug may stabilize the formulation, attenuating the effect of temperature change on NLC. As observed in previous studies, small differences in the lipid composition might considerably impact the zeta potential and, consequently, the quality of the nanoparticles [60].

Table 7
Thermal Properties ITF3756-NLC and plain NLC, including the melting temperature (Tm) of all the peaks during heating and the associated enthalpy ΔH. When more than one peak is present, they are so close that the ΔH is integrated into all of them. A prediction is also formulated considering NLC comprises only a 2:1 proportion of Precirol and Transcutol. Crystallization temperatures during cooling (Tc) are also shown but discussed to a lesser extent since kinetic factors influence them more.

	T_m, °C	ΔH, J/g	Tc, °C	T_m, °C	ΔH, J/g
Precirol	56.7 ± 0.2	160 ± 5	53.4 ± 0.2	50.1; 56.8	143 ± 5
NLC	46.0 ± 0.2; 55.1 ± 0.2	127 ± 5	54.6 ± 0.2; 33.0 ± 0.2	50.0 ± 0.2; 58.3 ± 0.2	77 ± 5
ITF3756-NLC	51.1 ± 0.2	102 ± 5	55.7 ± 0.2; 34.3 ± 0.2	51.1 ± 0.2; 57.9 ± 0.2	81 ± 5
prediction	56.7 ± 0.2	107 ± 5	53.4 ± 0.2	50.1 ± 0.2; 56.8 ± 0.2	95 ± 5

In the case of ITF3756-NLC, the DSC thermogram indicated the existence of a single polymorphic form of the solid lipid in the molecular dispersion of the drug in the NLC matrix.

3.3. *In vitro studies on cellular models*

A375, A549, and Gli36ΔEGFR-2 cell lines from melanoma, lung, and brain, respectively, were used to evaluate the cellular viability of the unloaded NLC and the ITF3756-NLC. Also, the ability of ITF3756-NLC to increase the α-tubulin acetylation was studied using the same cell lines.

3.3.1. *Cell viability assay*

The impact of NLC on cellular viability was determined by using an MTT assay to evaluate the applicability of these optimized carriers in a biological environment. Fig. 9a shows the effect of increasing NLC concentration along with the three cell lines A375, A549 and Gli36-ΔEGFR-2.

NLC doses up to 40E10 NP/mL seem well tolerated by all the cell lines tested since the cell viability was >50 %. On the other hand, NLC doses ≥150E10 induced a substantial reduction in cell viability for A549 and Gli36ΔEGFR-2 and are non-toxic for A375 cells up to 80E10 NP/mL. It is essential to highlight that the different cell types used showed different responses to the NLC treatment (i.e. when treated with 80E10 NP/mL). Therefore, cell responsiveness to the carrier must be considered in the design of nanoparticles for drug delivery. The 40E10 NP/mL concentration was used as a reference in the experiments to evaluate if ITF3756 retains its pharmacological activity after loading in NLC.

As ITF3756 as a free drug has no effect on the cellular viability in all three cell lines (Fig. 11S, Supplementary Information), we cannot use the MTT assay to access the biological activity of the drug, i.e., if the drug conserved its biological activity. For that, the determination of α-tubulin acetylation levels by Western Blot (WB) was carried out to evaluate the target engagement of the HDAC6i. The chosen ITF3756 concentration considered as free or loaded in the NLC was 2.5 μM (Fig. 9b), a concentration in which 40E10 NP/mL of NLC (cell viability higher than 50 %) provided cell viability for the ITF3756-NLC also higher than 50 %, even though previous studies with other cell lines showed HDAC6 selective inhibitors display cytotoxicity above 1 μM [11].

3.3.2. *Immunoblot analysis*

The *in vitro* ability of ITF3756 to increase the α-tubulin acetylation after incorporation in NLC was checked in three cancer cell lines. Fig. 10 shows that the acetylation levels of α-tubulin increased in every cell line treated with free ITF3756 (see Fig. 12S, Supplementary Information, for the original blots). HDAC6 can be mainly found in the cytoplasm, where it deacetylases non-histonic targets like tubulin. Here, when HDAC is inhibited, acetylation increases, which is mediated by the enzymatic counterparts (histone acetyltransferases). The acetylation of α -tubulin is used to assess the target efficacy due to the inhibition of HDAC6 that determines an increase of α-tubulin acetylation and a consequent signal cascade that eventually mediates the anti-tumor effect. The total α-tubulin was used as a normalization protein to adjust the quantity of acetylated tubulin over the total and assess how much it increased after the treatment without a particular ratio to achieve; generally, the more it is increased, the more HDAC6 is inhibited.

The pharmacological activity of ITF3756 was also maintained after NCL loading, as shown by the increase of the acetylation levels of α-tubulin in all cell lines treated with ITF3756-NLC. More interestingly, the ITF3756 effect was enhanced when entrapped in NLC, thus showing that the NLC could promote a better HDAC inhibitor delivery.

4. Conclusions

DOE and RSM were used to design NLC to facilitate the delivery of a poorly soluble HDAC inhibitor — a promising drug candidate for cancer immunotherapy. The designed ITF3756-NLC exhibited favorable physicochemical properties and long-term stability. The presence of ITF3756 in the NLC does not destabilize the assembly and instead helps obtain an intimate mixing of components, thus increasing the particle viability at RT. The formulation volume played an essential role in the PDI, thus being a crucial factor for a future scale-up of this NLC formulation. Additionally, the ITF3756-NLC demonstrated excellent biocompatibility and preserved the pharmacological properties of the encapsulated drug, further enhancing its potential for therapeutic application.

Funding

This study was funded by the project IMMUN-HUB “Sviluppo di nuove molecole di seconda generazione per immunoterapia oncologica”, CUP E51B19000550007–Call HUB Ricerca e Innovazione, cofunded by POR FESR 2014–2020 (Regional Operational Programme, European Regional Development Fund)]. M.M. thanks the support from the Italian Ministry of University and Research (MIUR) through the Dipartimento di Eccellenza – 2019 grant.

CRediT authorship contribution statement

Marcelo Kravicz: Writing – review & editing, Writing – original draft, Methodology, Investigation, Conceptualization. **Lorenzo Taiarol:** Methodology, Investigation. **Juliana S.R. Viegas:** Writing – review & editing, Methodology. **Giulia Sierri:** Investigation. **Michele Mauri:** Methodology, Investigation. **Marcus Koch:** Methodology, Investigation. **Christian Steinkühler:** Investigation. **Francesca Re:** Writing – review & editing, Supervision, Resources, Project administration, Conceptualization.

Declaration of competing interest

The authors declare that they have no known competing financial interests or personal relationships that could have appeared to influence the work reported in this paper.

Data availability

Data will be made available on request.

Acknowledgements

We thank Dr Silvia Valtorta from the Experimental Imaging Center, IRCCS San Raffaele Scientific Institute, Milan, Italy. In addition, we thank Prof. Domenico Mallardo from Istituto Nazionale Tumori - IRCCS - Fondazione "G. Pascale", Naples, Italy, for the cells used in this study.

Appendix A. Supplementary data

Supplementary data to this article can be found online at https://doi.org/10.1016/j.jddst.2024.106238.

References

[1] T.C.S. Ho, A.H.Y. Chan, A. Ganesan, Thirty years of HDAC inhibitors: 2020 insight and hindsight, J. Med. Chem. 63 (2020) 12460–12484, https://doi.org/10.1021/acs.jmedchem.0c00830.

[2] G. Sandrone, C.D. Cukier, K. Zrubek, M. Marchini, B. Vergani, G. Caprini, G. Fossati, C. Steinkühler, A. Stevenazzi, Role of fluorination in the histone deacetylase 6 (HDAC6) selectivity of benzohydroxamate-based inhibitors, ACS Med. Chem. Lett. 12 (2021) 1810–1817, https://doi.org/10.1021/acsmedchemlett.1c00425.

[3] C. Zhao, H. Dong, Q. Xu, Y. Zhang, Histone deacetylase (HDAC) inhibitors in cancer: a patent review (2017-present), Expert Opin, Ther. Pat. 30 (2020) 263–274, https://doi.org/10.1080/13543776.2020.1725470.

[4] X.H. Zhang, Qin-Ma, H.P. Wu, M.Y. Khamis, Y.H. Li, L.Y. Ma, H.M. Liu, A review of progress in histone deacetylase 6 inhibitors Research: structural specificity and functional diversity, J. Med. Chem. 64 (2021) 1362–1391, https://doi.org/10.1021/acs.jmedchem.0c01782.

[5] R.R. Lim, A. Tan, Y.-C. Liu, V.A. Barathi, R.R. Mohan, J.S. Mehta, S.S. Chaurasia, ITF2357 transactivates Id3 and regulate TGFβ/BMP7 signaling pathways to attenuate corneal fibrosis, Sci. Rep. 6 (2016) 20841, https://doi.org/10.1038/srep20841.

[6] S. Galimberti, M. Canestraro, H. Savli, G.A. Palumbo, D. Tibullo, B. Nagy, S. Piaggi, F. Guerrini, N. Cine, M.R. Metelli, M. Petrini, ITF2357 interferes with apoptosis and inflammatory pathways in the HL-60 model: a gene expression study, Anticancer Res. 30 (2010) 4525–4535. http://www.ncbi.nlm.nih.gov/pubmed/21115902.

[7] L. Taiarol, C. Bigogno, S. Sesana, M. Kravicz, F. Viale, E. Pozzi, L. Monza, V. A. Carozzi, C. Meregalli, S. Valtorta, R.M. Moresco, M. Koch, F. Barbugian, L. Russo, G. Dondio, C. Steinkühler, F. Re, Givinostat-liposomes: anti-tumor effect on 2D and 3D glioblastoma models and pharmacokinetics, Cancers 14 (2022), https://doi.org/10.3390/cancers14122978.

[8] F. Leoni, G. Fossati, E.C. Lewis, J.-K. Lee, G. Porro, P. Pagani, D. Modena, M. L. Moras, P. Pozzi, L.L. Reznikov, B. Siegmund, G. Fantuzzi, C.A. Dinarello, P. Mascagni, The histone deacetylase inhibitor ITF2357 reduces production of pro-inflammatory cytokines in vitro and systemic inflammation in vivo, Mol. Med. 11 (2005) 1–15, https://doi.org/10.2119/2006-00005.Dinarello.

[9] A.M. Savino, J. Sarno, L. Trentin, M. Vieri, G. Fazio, M. Bardini, C. Bugarin, G. Fossati, K.L. Davis, G. Gaipa, S. Izraeli, L.H. Meyer, G.P. Nolan, A. Biondi, G. Te Kronnie, C. Palmi, G. Cazzaniga, The histone deacetylase inhibitor givinostat (ITF2357) exhibits potent anti-tumor activity against CRLF2-rearranged BCP-ALL, Leukemia 31 (2017) 2365–2375, https://doi.org/10.1038/leu.2017.93.

[10] S.A. Ganai, Histone deacetylase inhibitor givinostat: the small-molecule with promising activity against therapeutically challenging haematological malignancies, J. Chemother. 28 (2016) 247–254, https://doi.org/10.1080/1120009X.2016.1145375.

[11] F. Marampon, F. Leoni, A. Mancini, I. Pietrantoni, S. Codenotti, F. Letizia, F. Megiorni, G. Porro, E. Galbiati, P. Pozzi, P. Mascagni, A. Budillon, R. Maggio, V. Tombolini, A. Fanzani, G.L. Gravina, C. Festuccia, Histone deacetylase inhibitor ITF2357 (givinostat) reverts transformed phenotype and counteracts stemness in in vitro and in vivo models of human glioblastoma, J. Cancer Res. Clin. Oncol. 145 (2019) 393–409, https://doi.org/10.1007/s00432-018-2800-8.

[12] S. Pulya, S.A. Amin, N. Adhikari, S. Biswas, T. Jha, B. Ghosh, HDAC6 as privileged target in drug discovery: a perspective, Pharmacol. Res. 163 (2021) 105274, https://doi.org/10.1016/j.phrs.2020.105274.

[13] Y. Li, E. Seto, HDACs and HDAC inhibitors in cancer development and therapy, Cold Spring Harb. Perspect. Med. 6 (2016) 1–34, https://doi.org/10.1101/cshperspect.a026831.

[14] T. Qiu, L. Zhou, W. Zhu, T. Wang, J. Wang, Y. Shu, P. Liu, Effects of treatment with histone deacetylase inhibitors in solid tumors: a review based on 30 clinical trials, Future Oncol. 9 (2013) 255–269, https://doi.org/10.2217/fon.12.173.

[15] Y.C. Zheng, H.Q. Kang, B. Wang, Y.Z. Zhu, M.A.A. Mamun, L.F. Zhao, H.Q. Nie, Y. Liu, L.J. Zhao, X.N. Zhang, M.M. Gao, D.D. Jiang, H.M. Liu, Y. Gao, Curriculum vitae of HDAC6 in solid tumors, Int. J. Biol. Macromol. 230 (2023) 123219, https://doi.org/10.1016/j.ijbiomac.2023.123219.

[16] A.M. Tsimberidou, P.A. Beer, C.A. Cartwright, C. Haymaker, H.H. Vo, S. Kiany, A. R.L. Cecil, J. Dow, K. Haque, F.A. Silva, L. Coe, H. Berryman, E.A. Bone, G. M. Nogueras-Gonzalez, D. Vining, H. McElwaine-Johnn, I.I. Wistuba, Preclinical development and first-in-human study of KA2507, a selective and potent inhibitor of histone deacetylase 6, for patients with refractory solid tumors, Clin. Cancer Res. 27 (2021) 3584–3594, https://doi.org/10.1158/1078-0432.CCR-21-0238.

[17] J. Yoo, Y.H. Jeon, D.H. Lee, G.W. Kim, S.W. Lee, S.Y. Kim, J. Park, S.H. Kwon, HDAC6-selective inhibitors enhance anticancer effects of paclitaxel in ovarian cancer cells, Oncol. Lett. 21 (2021) 1–11, https://doi.org/10.3892/ol.2021.12462.

[18] X. Peng, L. Li, J. Chen, Y. Ren, J. Liu, Z. Yu, H. Cao, J. Chen, Discovery of novel histone deacetylase 6 (HDAC6) inhibitors with enhanced antitumor immunity of anti-PD-L1 immunotherapy in melanoma, J. Med. Chem. 65 (2022) 2434–2457, https://doi.org/10.1021/acs.jmedchem.1c01863.

[19] A. Manuscript, Yeast to mice and men, Mol. Cell. 9 (2009) 206–218, https://doi.org/10.1038/nrm2346.The.

[20] J. Auzmendi-Iriarte, A. Saenz-Antoñanzas, I. Mikelez-Alonso, E. Carrasco-Garcia, M. Tellaetxe-Abete, C.H. Lawrie, N. Sampron, A.L. Cortajarena, A. Matheu, Characterization of a new small-molecule inhibitor of HDAC6 in glioblastoma, Cell Death Dis. 11 (2020), https://doi.org/10.1038/s41419-020-2586-x.

[21] B. Vergani, G. Sandrone, M. Marchini, C. Ripamonti, E. Cellupica, E. Galbiati, G. Caprini, G. Pavich, G. Porro, I. Rocchio, M. Lattanzio, M. Pezzuto, M. Skorupska, P. Cordella, P. Pagani, P. Pozzi, R. Pomarico, D. Modena, F. Leoni, R. Perego, G. Fossati, C. Steinkühler, A. Stevenazzi, Novel benzohydroxamate-based potent and selective histone deacetylase 6 (HDAC6) inhibitors bearing a pentaheterocyclic scaffold: design, synthesis, and biological evaluation, J. Med. Chem. 62 (2019) 10711–10739, https://doi.org/10.1021/acs.jmedchem.9b01194.

[22] V. Cervera-Carrascon, M. Siurala, J.M. Santos, R. Havunen, S. Tähtinen, P. Karell, S. Sorsa, A. Kanerva, A. Hemminki, 34th annual meeting & pre-conference programs of the society for immunotherapy of cancer (SITC 2019): part 2, J. Immunother. Cancer 7 (2019) 283, https://doi.org/10.1186/s40425-019-0764-0.

[23] V.R. Salvi, P. Pawar, Nanostructured lipid carriers (NLC) system: a novel drug targeting carrier, J. Drug Deliv. Sci. Technol. 51 (2019) 255–267, https://doi.org/10.1016/j.jddst.2019.02.017.

[24] M. Cirri, L. Maestrini, F. Maestrelli, N. Mennini, P. Mura, C. Ghelardini, L.D. C. Mannelli, Design, characterization and in vivo evaluation of nanostructured lipid carriers (NLC) as a new drug delivery system for hydrochlorothiazide oral administration in pediatric therapy, Drug Deliv. 25 (2018) 1910–1921, https://doi.org/10.1080/10717544.2018.1529209.

[25] S. Weber, A. Zimmer, J. Pardeike, Solid lipid nanoparticles (SLN) and nanostructured lipid carriers (NLC) for pulmonary application: a review of the state of the art, Eur. J. Pharm. Biopharm. 86 (2014) 7–22, https://doi.org/10.1016/j.ejpb.2013.08.013.

[26] J. Pardeike, A. Hommoss, R.H. Müller, Lipid nanoparticles (SLN, NLC) in cosmetic and pharmaceutical dermal products, Int. J. Pharm. 366 (2009) 170–184, https://doi.org/10.1016/j.ijpharm.2008.10.003.

[27] T.S. Patil, A.S. Deshpande, Nanostructured lipid carriers-based drug delivery for treating various lung diseases: a State-of-the-Art Review, Int. J. Pharm. 547 (2018) 209–225, https://doi.org/10.1016/j.ijpharm.2018.05.070.

[28] C.P. Costa, J.N. Moreira, J.M. Sousa Lobo, A.C. Silva, Intranasal delivery of nanostructured lipid carriers, solid lipid nanoparticles and nanoemulsions: a current overview of in vivo studies, Acta Pharm. Sin. B 11 (2021) 925–940, https://doi.org/10.1016/j.apsb.2021.02.012.

[29] J. Chen, H. Chen, S. Cui, B. Xue, J. Tian, S. Achilefu, Y. Gu, Glucosamine derivative modified nanostructured lipid carriers for targeted tumor delivery, J. Mater. Chem. 22 (2012) 5770–5783, https://doi.org/10.1039/c2jm15830b.

[30] D. Zhang, W. Dai, C. Duan, L. Jia, Y. Wang, F. Feng, Q. Zhang, Preparation and characteristics of oridonin-loaded nanostructured lipid carriers as a controlled-release delivery system, J. Microencapsul. 27 (2010) 234–241, https://doi.org/10.3109/02652040903079526.

[31] S. Das, A.B.H. Wong, Stabilization of ferulic acid in topical gel formulation via nanoencapsulation and pH optimization, Sci. Rep. 10 (2020) 1–18, https://doi.org/10.1038/s41598-020-68732-6.

[32] S. Das, W.K. Ng, P. Kanaujia, S. Kim, R.B.H. Tan, Formulation design, preparation and physicochemical characterizations of solid lipid nanoparticles containing a hydrophobic drug: effects of process variables, Colloids Surfaces B Biointerfaces 88 (2011) 483–489, https://doi.org/10.1016/j.colsurfb.2011.07.036.

[33] R. Tantra, P. Schulze, P. Quincey, Effect of nanoparticle concentration on zeta-potential measurement results and reproducibility, Particuology 8 (2010) 279–285, https://doi.org/10.1016/j.partic.2010.01.003.

[34] X. Xu, M.A. Khan, D.J. Burgess, A two-stage reverse dialysis in vitro dissolution testing method for passive targeted liposomes, Int. J. Pharm. 426 (2012) 211–218, https://doi.org/10.1016/j.ijpharm.2012.01.030.

[35] J.P. O'Shea, P. Augustijns, M. Brandl, D.J. Brayden, J. Brouwers, B.T. Griffin, R. Holm, A.C. Jacobsen, H. Lennernäs, Z. Vinarov, C.M. O'Driscoll, Best practices in current models mimicking drug permeability in the gastrointestinal tract - an UNGAP review, Eur. J. Pharm. Sci. 170 (2022), https://doi.org/10.1016/j.ejps.2021.106098.

[36] J. Basso, M. Mendes, T. Cova, J. Sousa, A. Pais, A. Fortuna, R. Vitorino, C. Vitorino, A stepwise framework for the systematic development of lipid nanoparticles, Biomolecules 12 (2022) 1–16, https://doi.org/10.3390/biom12020223.

[37] P. Mura, F. Maestrelli, M. D'Ambrosio, C. Luceri, M. Cirri, Evaluation and comparison of solid lipid nanoparticles (SLNs) and nanostructured lipid carriers (NLCs) as vectors to develop hydrochlorothiazide effective and safe pediatric oral liquid formulations, Pharmaceutics 13 (2021), https://doi.org/10.3390/pharmaceutics13040437.

[38] L. Séguy, A.C. Groo, D. Goux, D. Hennequin, A. Malzert-Fréon, Design of non-haemolytic nanoemulsions for intravenous administration of hydrophobic APIs, Pharmaceutics 12 (2020) 1–20, https://doi.org/10.3390/pharmaceutics12121141.

[39] M. Tavares Luiz, J. Santos Rosa Viegas, J. Palma Abriata, F. Viegas, F. Testa Moura de Carvalho Vicentini, M.V. Lopes Badra Bentley, M. Chorilli, J. Maldonado Marchetti, D.R. Tapia-Blácido, Design of experiments (DoE) to develop and to optimize nanoparticles as drug delivery systems, Eur. J. Pharm. Biopharm. 165 (2021) 127–148, https://doi.org/10.1016/j.ejpb.2021.05.011.

[40] M. Agrawal, S. Saraf, M. Pradhan, R.J. Patel, G. Singhvi, Ajazuddin, A. Alexander, Design and optimization of curcumin loaded nano lipid carrier system using Box-Behnken design, Biomed. Pharmacother. 141 (2021) 111919, https://doi.org/10.1016/j.biopha.2021.111919.

[41] C. Thapa, A. Ahad, M. Aqil, S.S. Imam, Y. Sultana, Formulation and optimization of nanostructured lipid carriers to enhance oral bioavailability of telmisartan using

Box–Behnken design, J. Drug Deliv. Sci. Technol. 44 (2018) 431–439, https://doi.org/10.1016/j.jddst.2018.02.003.
[42] Y. He, L. Luo, S. Liang, M. Long, H. Xu, Influence of probe-sonication process on drug entrapment efficiency of liposomes loaded with a hydrophobic drug, Int. J. Polym. Mater. Polym. Biomater. 68 (2019) 193–197, https://doi.org/10.1080/00914037.2018.1434651.
[43] M. Dükkanci, M. Vinatoru, T.J. Mason, Sonochemical treatment of Orange II using ultrasound at a range of frequencies and powers, J. Adv. Oxid. Technol. 15 (2012) 277–283, https://doi.org/10.1515/jaots-2012-0205.
[44] Y. Asakura, K. Yasuda, Frequency and power dependence of the sonochemical reaction, Ultrason. Sonochem. 81 (2021) 105858, https://doi.org/10.1016/j.ultsonch.2021.105858.
[45] S. Pimentel-Moral, M.C. Teixeira, A.R. Fernandes, I. Borrás-Linares, D. Arráez-Román, A. Martínez-Férez, A. Segura-Carretero, E.B. Souto, Polyphenols-enriched Hibiscus sabdariffa extract-loaded nanostructured lipid carriers (NLC): optimization by multi-response surface methodology, J. Drug Deliv. Sci. Technol. 49 (2019) 660–667, https://doi.org/10.1016/j.jddst.2018.12.023.
[46] S.S. Hallan, M. Sguizzato, E. Esposito, R. Cortesi, Challenges in the physical characterization of lipid nanoparticles, Pharmaceutics 13 (2021) 1–31, https://doi.org/10.3390/pharmaceutics13040549.
[47] N. Izza, N. Watanabe, Y. Okamoto, K. Suga, Y. Wibisono, N. Kajimura, K. Mitsuoka, H. Umakoshi, Dependence of the core-shell structure on the lipid composition of nanostructured lipid carriers: implications for drug carrier design, ACS Appl. Nano Mater. 5 (2022) 9958–9969, https://doi.org/10.1021/acsanm.2c02214.
[48] E. Esposito, M. Drechsler, P. Mariani, F. Carducci, M. Servadio, F. Melancia, P. Ratano, P. Campolongo, V. Trezza, R. Cortesi, C. Nastruzzi, Lipid nanoparticles for administration of poorly water soluble neuroactive drugs, Biomed. Microdevices 19 (2017), https://doi.org/10.1007/s10544-017-0188-x.
[49] R. Simonutti, D. Bertani, R. Marotta, S. Ferrario, D. Manzone, M. Mauri, M. Gregori, A. Orlando, M. Masserini, Morphogenic effect of common solvent in the self-assembly behavior of amphiphilic PEO-b-PLA, Polymer (Guildf). 218 (2021) 123511, https://doi.org/10.1016/j.polymer.2021.123511.
[50] M. Blomenhofer, S. Ganzleben, D. Hanft, H.W. Schmidt, M. Kristiansen, P. Smith, K. Stoll, D. Mäder, K. Hoffmann, "Designer" nucleating agents for polypropylene, Macromolecules 38 (2005) 3688–3695, https://doi.org/10.1021/ma0473317.
[51] A. Gordillo-Galeano, A. Ponce, C.E. Mora-Huertas, In vitro release behavior of SLN, NLC, and NE: an explanation based on the particle structure and carried molecule location, J. Drug Deliv. Sci. Technol. 76 (2022) 103768, https://doi.org/10.1016/j.jddst.2022.103768.
[52] I.V. Zelepukin, O.Y. Griaznova, K.G. Shevchenko, A.V. Ivanov, E.V. Baidyuk, N. B. Serejnikova, A.B. Volovetskiy, S.M. Deyev, A.V. Zvyagin, Flash drug release from nanoparticles accumulated in the targeted blood vessels facilitates the tumour treatment, Nat. Commun. 13 (2022) 1–15, https://doi.org/10.1038/s41467-022-34718-3.
[53] A.K. Jain, S. Thareja, In vitro and in vivo characterization of pharmaceutical nanocarriers used for drug delivery, Artif. Cells, Nanomedicine Biotechnol. 47 (2019) 524–539, https://doi.org/10.1080/21691401.2018.1561457.
[54] E.B. Souto, J.F. Fangueiro, A.R. Fernandes, A. Cano, E. Sanchez-Lopez, M.L. Garcia, P. Severino, M.O. Paganelli, M.V. Chaud, A.M. Silva, Physicochemical and biopharmaceutical aspects influencing skin permeation and role of SLN and NLC for skin drug delivery, Heliyon 8 (2022) e08938, https://doi.org/10.1016/j.heliyon.2022.e08938.
[55] S.A. Abouelmagd, B. Sun, A.C. Chang, Y.J. Ku, Y. Yeo, Release kinetics study of poorly water-soluble drugs from nanoparticles: are we doing it right? Mol. Pharm. 12 (2015) 997–1003, https://doi.org/10.1021/mp500817h.
[56] D.F. de Andrade, C. Zuglianello, A.R. Pohlmann, S.S. Guterres, R.C.R. Beck, Assessing the in vitro drug release from lipid-core nanocapsules: a new strategy combining dialysis sac and a continuous-flow system, AAPS PharmSciTech 16 (2015) 1409–1417, https://doi.org/10.1208/s12249-015-0330-0.
[57] D. Solomon, N. Gupta, N.S. Mulla, S. Shukla, Y.A. Guerrero, V. Gupta, Role of in vitro release methods in liposomal formulation development: challenges and regulatory perspective, AAPS J. 19 (2017) 1669–1681, https://doi.org/10.1208/s12248-017-0142-0.
[58] C. Freitas, R.H. Müller, Effect of light and temperature on zeta potential and physical stability in solid lipid nanoparticle (SLN®) dispersions, Int. J. Pharm. 168 (1998) 221–229, https://doi.org/10.1016/S0378-5173(98)00092-1.
[59] W. Pornputtapitak, J. Pantakitcharoenkul, V. Teeranachaideekul, K. Sinthiptharakoon, C. Sapcharoenkun, B. Meemuk, Effect of oil content on physiochemical characteristics of γ-oryzanol-loaded nanostructured lipid carriers, J. Oleo Sci. 68 (2019) 699–707, https://doi.org/10.5650/jos.ess18127.
[60] W. Mehnert, Solid lipid nanoparticles Production, characterization and applications, Adv. Drug Deliv. Rev. 47 (2001) 165–196, https://doi.org/10.1016/S0169-409X(01)00105-3.
[61] P.A. Makoni, K.W. Kasongo, R.B. Walker, Short term stability testing of efavirenz-loaded solid lipid nanoparticle (SLN) and nanostructured lipid carrier (NLC) dispersions, Pharmaceutics 11 (2019), https://doi.org/10.3390/pharmaceutics11080397.
[62] V.H. Nguyen, V.N. Thuy, T.V. Van, A.H. Dao, B.J. Lee, Nanostructured lipid carriers and their potential applications for versatile drug delivery via oral administration, OpenNano 8 (2022) 100064, https://doi.org/10.1016/j.onano.2022.100064.
[63] C.H. Loo, M. Basri, R. Ismail, H.L.N. Lau, B.A. Tejo, M.S. Kanthimathi, H.A. Hassan, Y.M. Choo, Effect of compositions in nanostructured lipid carriers (NLC) on skin hydration and occlusion, Int. J. Nanomedicine. 8 (2013) 13–22, https://doi.org/10.2147/IJN.S35648.